Postprint

Electrochromic Iridium-Containing Nickel Oxide Films with Excellent Electrochemical Cycling Performance

Rui-Tao Wen,[z] Gunnar A. Niklasson and Claes G. Granqvist*

Department of Engineering Sciences, The Ångström Laboratory, Uppsala University

P. O. Box 534, SE-75121 Uppsala, Sweden

Abstract

Electrochromic Ni oxide thin films attract much interest because of their large potential for applications as optically active layers in energy-saving and comfort enhancing smart windows in buildings. However Ni oxide, typically being the anodic counter electrode in a W-oxide-based device, may suffer severe charge capacity degradation upon extended electrochemical cycling. It is therefore important to identify improved Ni-oxide-based thin films for electrochromics. Here we describe a new class of such films wherein an addition of a small amount of Ir to Ni oxide is found to provide strongly improved electrochemical cycling durability. Best properties were achieved with $Ir/(Ir + Ni) = 7.6\%$, and such films displayed charge capacity and optical modulation that, remarkably, were still increasing after 10,000 cycles.

Keywords: Electrochromic, Ir-Ni oxide, thin films, durability.

* Electrochemical Society Active Member.

[z] Corresponding author: Ruitao.Wen@angstrom.uu.se

1. Introduction

A huge part of the world's primary energy is used in buildings. This part is as large as 30–40% on a global scale and is required for heating, cooling, lighting, ventilation, and appliances.[1] The fraction tends to increase—particularly in the richer countries—and 34, 36, 38 and 41% of the primary energy in the US was used in buildings in 1980, 1990, 2000 and 2010, respectively.[2] Clearly a lowering of the buildings' energy expenditure is important for diminishing the CO_2 release to the atmosphere and therefore for curtailing risks associated with global warming, increasing sea level, etc.[3] The buildings sector is noteworthy for its great savings potential, which is largely untapped as a consequence of poor but well entrenched practices.[4] In particular glazings—encompassing windows and glass facades—tend to be weak links in the buildings' energy system and frequently let in or out too much energy[5] which must be balanced by energy guzzling cooling or heating. The desired control of the energy throughput can be achieved by electrochromic (EC) glazings,[6, 7] which can lead to significant energy savings[8–11] combined with glare control without loss of precious visual indoors–outdoors contact.

The most widely studied and implemented EC devices consist of five superimposed layers on a single transparent substrate or positioned between two transparent substrates.[7, 12] The central layer is an electrolyte—typically an oxide-based ion conducting thin film or a polymer electrolyte—which joins two EC layers one of which colors under charge insertion (cathodically) and the other coloring under charge extraction (anodically). This three-layer arrangement is surrounded by transparent electrical conductors. The optical properties of the window are changed persistently and reversibly when a voltage is applied between the transparent electrodes so that charge is shuttled between the cathodic and anodic layers.

The *cathodic* EC layer in today's EC "smart" windows for buildings[12] is usually based on tungsten oxide, which can have excellent properties if ion insertion and extraction is exercised

in an appropriate potential range.[7] The *anodic* side of the device has been subject to much inquiry. Pure iridium oxide was employed in some early devices[7] for printing alphanumeric information on analog photographic film and also for anti-dazzling rear-view mirrors for automobiles, but obviously this material is too expensive for large-area applications even if diluted with less costly oxides based on tin[13, 14] or tantalum.[15–18] Ni oxide was put forward as an alternative[19, 20] and has been of sustained interest for almost 30 years. We recently demonstrated that the coloration is a surface process[21] and that the degradation of charge density in Ni oxide obeys a power law[22] upon cycling in a Li-conducting electrolyte, which implies that a monotonic decline of the optical properties takes place and eventually leads to device failure. Many studies during the last years have focused on ways to improve the performance of Ni oxide films with regard to optical modulation speed and span, bleached-state transmittance and electrochemical cycling durability by use of additives such as Li,[23–25] C,[26, 27] N,[28] F,[29] Al,[30] Ti,[31, 32] V,[33, 34] Mn,[35] Co,[36] Cu,[37] W,[38, 39] (Li,W),[40] (Li,Al),[41] (Li,Zr),[42] and LiPON.[43] Nevertheless important challenges remain for Ni-oxide-based films and limit the performance of today's EC smart windows.

Here, we report on a novel Ni-oxide-based anodic EC layer that can overcome the charge density degradation of pure nickel oxide in a Li-based electrolyte. This is accomplished by adding a *small* amount of Ir to the Ni oxide. The Ir–Ni oxide films were made by reactive dc magnetron co-sputtering in argon–oxygen atmosphere, which is a scalable technique well suited for large-area deposition.[44] Some preliminary results of this study were presented recently.[45]

2. Experimental section

Thin films of Ir–Ni oxide were made by reactive dc magnetron sputtering in a multi-target coating system based on a Balzers UTT 400 unit. Both nickel (99.95%) and iridium (99.95%)

targets were 5-cm-diameter plates, and the target–substrate separation was 13 cm. Pre-sputtering took place in argon (99.998%) for two minutes, and oxygen (99.998%) was then introduced. The total pressure was maintained at ~4 Pa during sputtering. The power on the Ni target was kept at 200 W whereas the power on the Ir target was varied from 10 to 40 W in order to get different Ir/(Ir + Ni) ≡ γ atom ratios in the films. No substrate heating was used. Film uniformity was ensured by substrate rotation during the depositions. The substrates were glass plates with transparent and electrically conducting layers of In_2O_3:Sn (known as ITO) with a sheet resistance of 60 Ω. Before deposition, one edge of the ITO coated glass was covered by a narrow strip of Teflon tape in order to allow film thickness determination and to provide electrical contacts for subsequent electrochemical measurements. Films were also grown on carbon substrates for Rutherford Backscattering Spectrometry (RBS) studies.

Structural data on the Ir–Ni oxide films were determined by X-ray diffraction (XRD) using a Siemens D5000 diffractometer operating with Cu K_α radiation at a wavelength λ_x of 0.154 nm; these data were compared with the Joint Committee on Powder Diffraction Standards (JCDPS) data base. Grain sizes D of the films were determined from Scherrer's formula,[46] *i.e.*,

$$D = \frac{k\lambda_x}{\beta\cos\theta},$$

(1)

where $k \sim 0.9$ is a dimensionless "shape factor", β is the full width at half-maximum of an X-ray diffraction peak, and 2θ is the diffraction angle. Film morphology was characterized by scanning electron microscopy (SEM) using a LEO 1550 FEG Gemini instrument with an acceleration voltage of 10 kV and in-lens detector. Elemental compositions were determined by RBS at the Uppsala Tandem Laboratory, specifically using 2 MeV ^{4}He ions back scattered at an angle of 170°. The RBS data were fitted to a model of the film–substrate system by use of the SIMNRA program.[47] Film density ρ was computed from

$$\rho = \frac{MN_s}{n_{atoms}N_A d}, \tag{2}$$

where M is molar mass, N_s is thickness in atoms/cm^2, n_{atoms} is number of atoms in a molecule, N_A is Avogadro's constant, and d is film thickness. Film thicknesses were determined by surface profilometry using a DektakXT instrument and were found to be ~300 ± 20 nm.

X-ray photoelectron spectroscopy (XPS) was used to characterize the oxidation state for Ir in Ni oxide. We employed a PHI Quantum 2000 ESCA system with a monochromatic Al K$_\alpha$ radiation source. The pass energy was 23.5 eV, and the energy resolution was 0.1 eV for high-resolution scans. The C 1s peak at 284.8 eV was used to calibrate the binding energies. Shirley background was used for corrections of the XPS spectra.

The EC performance was evaluated in a three-electrode electrochemical cell by use of a computer-controlled ECO Chemie Autolab/GPES Interface. The Ir–Ni oxide films served as working electrode and were electrochemically cycled in electrolytes of 1 M LiClO$_4$ in propylene carbonate (LiClO$_4$–PC) using lithium metal foil as counter and reference electrodes. The voltage sweep rate was 50 mV/s. Cyclic voltammetry (CV) measurements for up to 10,000 cycles were performed in an argon-filled glove box at 20 °C. The charge density determined from the cyclic voltammetry data is given by

$$C = \int \frac{jdV}{s}, \tag{3}$$

where C is charge capacity (in units of mC cm^{-2}), j is current density (in mA cm^{-2}), s is scan rate (in V/s), and V is voltage (in V). Optical transmittance measurements were recorded *in situ* during electrochemical cycling of Ir–Ni oxide films in the 380–800 nm wavelength range by using a fiber-optical instrument from Ocean Optics. The electrochemical cell was positioned between a tungsten halogen lamp and the detector, and the 100-%-level was taken as the transmittance recorded before immersion of the sample in the electrolyte.

3. Results and discussion

3.1 Characterization of as-deposited films

Our investigation encompassed Ir–Ni oxide films with various compositions specified by γ as well as pure Ni oxide films. Photos of as-deposited films on glass indicate that the samples become darker upon increasing values of γ (Fig. S1 in the Electronic Supplementary Material), which suggests that the Ir concentration should be kept low not only for cost reasons but also in order to allow high optical transmittance and small color rendering.

Surface morphologies of as deposited films were studied by SEM (Fig. 1a, c; Fig. S2a–c). The films appear smooth and mostly exhibit an irregular pattern of narrow cracks separated by distances of ~0.2–1.0 μm. Data for films having undergone CV cycling are discussed later.

Compositional analyses by RBS gave clear evidence for the expected elements in the films, as well as for the carbon substrate, and showed that Ir is uniformly distributed in Ni oxide films so that unambiguous values can be given for γ (Fig. 2). Table 1 reports specific data on atomic compositions. No contamination was apparent. Film density was obtained from Eq. (2) and is shown in Fig. 3(a). Clearly the density increases almost in proportion with the films' Ir contents. Bulk NiO and IrO_2 have densities of 6.84 g cm^{-3} and 11.66 g cm^{-3}, respectively, which indicates that the sputter deposited Ir–Ni oxide films have considerable porosity.

Structural information was acquired by x-ray diffraction for the same samples as before and also for pure Ni oxide and for the ITO-coated glass substrate (Fig. 3b). All diffraction peaks for the Ir–Ni oxide films could be indexed to the $Fm\bar{3}m$ space group of cubic NiO (JCPDS No. 04-0835), and no traces of IrO_2 or metallic Ir-based phases were observed. The (111) peaks grow in relative intensity as γ is increased while the (200) peaks display a

6

corresponding drop; these changes point at a variation of the preferred orientation of the crystallites in the films. The film with the highest Ir fraction shows diminished crystallinity, as evidenced by its less distinct diffraction peaks, as well as by its small grain size (Fig. 3a). By comparing the various XRD patterns, we found small but unambiguous shifts of the (111), (200) and (220) diffraction peaks towards lower angles for enhanced Ir concentrations (Fig. 3c), which indicates increased lattice spacing. The cell volume for the Ir–Ni oxide has a concomitant increase and becomes slightly larger than that of pure Ni oxide. This observation is consistent with the expected change if Ir atoms (radius 0.180 nm) substitute Ni atoms (radius 0.149 nm)[48] or locate in interstitial positions.

The binding state of Ir was studied by XPS, and Fig. 4 shows data where features are assigned to 4f states of Ir^{3+} and Ir^{4+}. Specifically, the peaks corresponding to Ir $4f_{7/2}$ with binding energies of 62.2 and 63.9 eV correspond to Ir^{3+} and Ir^{4+}, respectively, whereas no trace of Ir^0 (metallic Ir) could be seen at 61.0 eV.[49-53] It is evident that Ir^{3+} is dominant at all compositions, and that a minor component of Ir^{4+} may be present at $\gamma = 18.3\%$. The broad XPS feature at ~67 eV is due to Ni 3p states.[54]

3.2 Charge density and electrochromism

The electrochromic properties of the Ir–Ni oxide films were evaluated and compared with those for pure Ni oxide. Specifically we performed cyclic voltammetry in Li–PC at a sweep rate of 50 mV/s. The potential range used here—*i.e.*, 2.0–4.1 V *vs*. Li/Li$^+$—was chosen in order to have good stability of the pure Ni oxide films.[22] The spread in film thickness among the various samples was small enough not to play any significant role for our results.

Cyclic voltammograms for thin films of Ni oxide and Ir–Ni oxide are shown in Fig. 5(a) and Fig. S3. Areas between the curves and the zero-current level represent inserted and

extracted charge density and were calculated according to Eq. 3. For the pure Ni oxide film, electrochemical cycling led to an initial fast drop of charge density followed by a much slower decline (Fig. 5b), which can be described in terms of a power law.[22] Clearly, all Ir–Ni oxide films exhibited remarkable electrochemical stability and withstood at least 10,000 CV cycles. Data for films with $\gamma = 4.5\%$ and $\gamma = 5.5\%$ have initial charge densities similar to that for pure Ni oxide, but the decline rate was much smaller. The magnitude of the charge density indicates that the electrochromism is probably due to surface processes in these films, as it is for Ni oxide.[21] We were unable document any influence of the Ir-dependent preferred crystallite orientation (*cf.* Fig. 3c).

Very interesting results emerged when the Ir content was increased still further, and the sample with $\gamma = 7.6\%$ showed, after an initial small drop, that the charge density increased approximately linearly upon CV cycling for up to 10,000 times. The sample with $\gamma = 8.8\%$ indicated a substantial increase of the charge density during the first cycles, which was followed by a pronounced roughly linear increase. The net increase was ~20% for the sample with $\gamma = 7.6\%$ and as much as ~70% for $\gamma = 8.8\%$ (Fig. 5b). When γ was further increased to 18.3%, the charge density went up rapidly during the initial CV cycling, then rose more gradually until reaching a peak at ~6,000 cycles, and declined slowly thereafter upon further cycling (Fig. 5b). The increase in charge capacity upon extended cycling indicates that not only the surface, but also a greater portion of the film, becomes accessible to ion intercalation. This is also indicated by the charge density for these Ir–Ni oxide films, which is obviously larger than for the pure Ni oxide film (Fig. 5b), although their thicknesses are roughly the same. As mentioned above, the larger cell volume resulting from increased interatomic spacing may facilitate ion-exchange. However, the difference in charge density among films of Ir–Ni oxide and Ni oxide is clearly related to the different shapes of their voltammograms, which may indicate different charge insertion and extraction processes. To be specific, most

charge insertion and extraction takes place at 2.7–4.1 V *vs*. Li/Li$^+$ for Ni oxide, whereas this insertion and extraction occurs in the whole potential range—*i.e*., at 2.0–4.1 V *vs*. Li/Li$^+$—for Ir–Ni oxide and becomes enlarged upon further increase of the Ir content in the films (Fig. 5a). It is probable that intercalation processes taking place in an Ir-containing phase at low potentials are involved, but the detailed mechanism is not yet known.

The increased charge densities upon CV cycling are correlated with significant changes in the crystallinity of the films. XRD data on the film with γ = 4.5% showed that the structure was barely altered after 10,000 cycles (Fig. 6a). However, by increasing γ to 5.4%, XRD data revealed that the relative diffraction intensities were increased upon prolonged cycling (Fig. S4a), which means that the crystalline structure of the film has become more ordered. XRD data on the sample with γ = 7.6% (Fig. 6b) shows that the crystallinity was greatly enhanced after 10,000 CV cycles, as inferred from the intensities of the (111) and (200) diffraction peaks. However, the peak width remained the same, and the crystallite size was D ~13 nm both initially and after cycling. For the sample with γ = 8.8%, the improvement of crystallinity was not as profound as for γ = 7.6%, but a slight increase of the diffraction intensity can be noted after CV cycling (Fig. S4b). Finally for the film with γ = 18.3%, a slight decrease of diffraction intensity is clearly visible after 10,000 CV cycles (Fig. 6c). XPS data were recorded on the film with γ = 7.6% before and after 10,000 CV cycles (Fig. S5). Clearly Ir^{3+} predominates, and the Ir^{4+} content is possibly increased after cycling.

We next discuss the optical properties and electrochromism in the Ir–Ni oxide films. The optical transmittance of the as-deposited films is significantly lower than for pure Ni oxide. In particular the spectra in Fig. 7 exhibit a steep decline towards shorter wavelengths below about 550 nm. The absorption increases with increasing Ir content and is probably due to both Ir-based and Ni-based oxide species.[7,21,55] For γ = 18.3% one may associate the lowered transmittance with an increased content of Ir^{4+} (*cf*. Fig. 4). It is noteworthy that the optical

modulation in the first CV cycle is very small for all films, in fact significantly smaller than for the pure Ni oxide film (Fig. 7a). In addition, the optical transmittance spectra reveal that the film with γ = 4.5% shows a very small optical modulation ($T_{bleach} - T_{colored}$) even after 10,000 CV cycles (Fig. 7b).

For the film with γ = 5.4%, the optical modulation is still small, but both T_{bleach} and $T_{colored}$ become larger than in the initial state after extended CV cycling (Fig. S6a). As the Ir content in the films is further enlarged, the optical modulation range displays an accompanying increase which is especially pronounced for γ = 7.6% (Fig. 7c). To the best of our knowledge, a *sustained cycle-dependent growth of charge density and electrochromic modulation* has not been reported before in any EC oxide. Regarding the most Ir–rich film, optical data showed that it has very little optical variation initially, whereas optical modulation as well as transmittance in bleached and colored states increased after CV cycling (Fig. 7d).

We also evaluated the Ir–Ni oxide films with an extended upper voltage limit, specifically in the range 2.0–4.4 V *vs*. Li/Li$^+$. All films then showed a peak in their charge density after ~1,000 to ~4,000 cycles, and the film with γ = 7.6 % still demonstrated superior long-term performance (Fig. 8). The other films, with various Ir concentrations, showed an earlier decrease of charge density than the film with an Ir content of 7.6 %. It is apparent that when the Ir concentration is larger than 7.6% (such as 8.8% or 18.3%) the films exhibit faster degradation of charge density. In the two studied potential ranges, 2.0–4.1 and 2.0–4.4 V *vs*. Li/Li$^+$, it seems that incorporation of 7.6% Ir into Ni oxide gives the best EC performance as regards both charge density stability (durability) and optical modulation.

Finally, scanning electron microscopy was employed to illustrate differences in the morphology of the Ir–Ni oxide films as a result of CV cycling for 10,000 times in the range of 2.0–4.1 V *vs*. Li/Li$^+$ (Fig. 1 and Fig. S2). The features in the as-deposited films remained

unchanged after cycling for films with γ being 4.5, 5.4 and 7.6%. The film with $\gamma = 8.8\%$ displayed some widening of the cracks after 10,000 cycles, whereas the film with $\gamma = 18.3\%$ was different and the cycled film had a rather regular pattern of ~0.1-μm-wide fissures separated by ~1 μm (Fig. 1d, e). It is possible that the decline of the charge density after ~6,000 CV cycles (Fig. 5b) is associated with the opening-up of these fissures.

4. Conclusion

Achieving stable, reversible anodic layers for electrochromic devices is one the main challenges in order to accomplish durable smart windows for large-scale applications. Here we have shown that Ir–Ni oxide, with a modest amount of Ir, can exhibit excellent durability during cycling in LiClO$_4$–PC. We also observed a *sustained cycle-dependent growth of both charge density and electrochromic modulation* which, as far as we know, has not been reported before in any electrochromic oxide, and our results hence introduce a new class of anodic materials for electrochromic devices. Putting Ir into Ni oxide leads to an increase of the lattice constant, which apparently opens up the structure and allows Li$^+$ insertion/ extraction in the films, accompanied by an increase in their degree of crystallinity. These effects are confined to small amounts of Ir, and Ir–Ni oxide films show mechanical failure at excessive Ir contents. It thus appears that superior electrochromism in Ir–Ni oxide is reached as a tradeoff between several properties.

Acknowledgments

References

1. UNEP, Buildings and Climate Change: Status, Challenges and Opportunities. *United Nations Environment Programme, Paris, France*, 2007.

2. US Department of Energy, Washington, DC, USA; http://buildingsdatabook.eere.energy.gov/.

3. Intergovernmental Panel on Climate Change. http://www.ipcc.ch.

4. B. Richter, D. Goldston, G. Crabtree, L. Glicksman, D. Goldstein, D. Greene, D. Kammen, M. Levine, M. Lubell, M. Savitz, D. Sperling, F. Schlachter, J. Scofield and J. Dawson, *Rev. Mod. Phys.* **80**, S1 (2008).

5. G. B. Smith and C. G. Granqvist, Green Nanotechnology: Solutions for Sustainability and Energy in the Built Environment, CRC Press, Boca Raton, FL, USA, 2010.

6. C. G. Granqvist, *Nat. Mater.* **5**, 89 (2006).

7. C. G. Granqvist, Handbook of Inorganic Electrochromic Materials. *Elsevier, Amsterdam, The Netherlands*, 1995.

8. E. S. Lee, S. E. Selkowitz, R. D. Clear, D. L. DiBartolomeo, J. H. Klems, L. L. Fernandes, G. J. Ward, V. Inkarojrit and M. Yazdanian, Advancement of Electrochromic Windows, California Energy Commission, PIER, CEC-500-2006-052, 2006.

9. D. T. Gillaspie, R. C. Tenent and A. C. Dillon, *J. Mater. Chem.* **20**, 9585 (2010).

10. N. DeForest, A. Shehabi, G. Garcia, J. Greenblatt, E. Masanet, E. S. Lee, S. Selkowitz and D. J. Milliron, *Building Environment* **61**, 160 (2013).

11. M. Pittaluga, in Eco-Efficient Materials for Mitigating Building Cooling Needs: Design, Properties and Applications, F. Pacheco-Torgal, J. Labrincha, L. F. Cabeza and C. G. Granqvist, editors, Woodhead, Cambridge, UK, 2015, Ch. 17, pp. 473–497.

12. C. G. Granqvist, *Thin Solid Films* **564**, 1 (2014).

13.   T. Niwa and O. Takai, *Thin Solid Films* **518**, 5340 (2010).

14.   T. Niwa and O. Takai, *Jpn. J. Appl. Phys.* **49**, 105802 (2010).

15.   J. Backholm, A. Azens and G. A. Niklasson, *Sol. Energy Mater. Sol. Cells* **90**, 414 (2006).

16.   J. Backholm and G. A. Niklasson, *Sol. Energy Mater. Sol. Cells* **92**, 1388 (2008).

17.   J. Backholm, E. Avendano, A. Azens, G. d. M. Azevedo, E. Coronel, G. A. Niklasson and C. G. Granqvist, *Sol. Energy Mater. Sol. Cells* **92**, 91 (2008).

18.   S. U. Yun, S. J. Yoo, J. W. Lim, S. H. Park, I. Y. Cha and Y.-E. Sung, *J. Electrochem. Soc.* **157**, J256 (2010).

19.   G. A. Niklasson and C. G. Granqvist, *J. Mater. Chem.* **17**, 127 (2007).

20.   J. S. E. M. Svensson and C. G. Granqvist, *Appl. Phys. Lett.* **49**, 1566 (1986).

21.   R.-T. Wen, C. G. Granqvist and G. A. Niklasson, *Adv. Funct. Mater.* **25**, 3359 (2015).

22.   R.-T. Wen, C. G. Granqvist and G. A. Niklasson, *Appl. Phys. Lett.* **105**, 163502 (2014).

23.   R. C. Tenent, D. T. Gillaspie, A. Miedaner, P. A. Parilla, C. J. Curtis and A. C. Dillon, *J. Electrochem. Soc.* **157**, H318 (2010).

24.   T. Kubo, Y. Nishikitani, Y. Sawai, H. Iwanaga, Y. Sato and Y. Shigesato, *J. Electrochem. Soc.* **156**, H629 (2009).

25.   H. Moulki, D. H. Park, B.-K. Min, H. Kwon, S.-J. Hwang, J.-H. Choy, T. Toupance, G. Campet and A. Rougier, *Electrochim. Acta* **74**, 46 (2012).

26.   Y.-S. Lin, D.-J. Lin, P.-J. Sung and S.-W. Tien, *Thin Solid Films* **532**, 36 (2013).

27.   Y.-S. Lin, D.-J. Lin, L.-Y. Chiu and S.-W. Lin, *J. Solid State Electrochem.* **16**, 2581 (2013).

28.   F. Lin, D. T. Gillaspie, A. C. Dillon, R. M. Richards and C. Engtrakul, *Thin Solid Films* **527**, 26 (2013).

29.   N. K. Shrestha, M. Yang and P. Schmuki, Electrochem. *Solid State Lett.* **13**, C21 (2010).

30.   D. Mondal and G. Villemure, *J. Electroanal. Chem.* **628**, 67 (2009).

31.   A. Al-Kahlout and M. A. Aegerter, *Sol. Energy Mater. Sol. Cells* **91**, 213 (2007).

32.   K. Zhang, X. Q. Zhang, C. X. Chang, S. J. Zhang, X. C. Wang, D. L. Sun and M. A. Aegerter, *Sol. Energy Mater. Sol. Cells* **114**, 192 (2013).

33.   Y.-S. Lin, P.-W. Chen and D.-J. Lin, *Thin Solid Films* **518**, 7416 (2010).

34.   J.-M. Ye, Y.-P. Lin, Y.-T. Yang, J.-T. Chang and J.-L. He, *Thin Solid Films* **519**, 1578 (2010).

35.   T. Yoshino, K. Kobayashi, S. Araki, K. Nakamura and N. Kobayashi, *Sol. Energy Mater. Sol. Cells* **99**, 43 (2012).

36.   K. K. Purushothaman and G. Muralidharan, *J. Non-Cryst. Solids* **358**, 354 (2012).

37.   L. Zhao, G. Su, W. Liu, L. Cao, J. Wang, Z. Dong and M. Song, *Appl. Surf. Sci.* **257**, 3974 (2011).

38.   S. V. Green, C. G. Granqvist and G. A. Niklasson, *Sol. Energy Mater. Sol. Cells* **126**, 248 (2014).

39.   S. V. Green, Electrochromic Nickel–Tungsten Oxides: Optical, Electrochemical and Structural Characterization of Sputter-Deposited Thin Films in the Whole Composition Range, PhD thesis, Digital Comprehensive Summaries of Uppsala Dissertations from the Faculty of Science and Technology 963, Uppsala, Sweden, 2012, ISBN 978-91-554-8444-6.

40.   D. Gillaspie, A. Norman, C. E. Tracy, J. R. Pitts, S.-H. Lee and A. Dillon, *J. Electrochem. Soc.* **157**, H328 (2010).

41.   F. Lin, D. Nordlund, T.-C. Weng, R. G. Moore, D. T. Gillaspie, A. C. Dillon, R. M. Richards and C. Engtrakul, *ACS Appl. Mater. Interfaces* **5**, 301 (2013).

42.   F. Lin, D. Nordlund, T.-C. Weng, D. Sokaras, K. M. Jones, R. B. Reed, D. T. Gillaspie, D. G. J. Weir, R. G. Moore, A. C. Dillon, R. M. Richards and C. Engtrakul, *ACS Appl. Mater. Interfaces* **5**, 3643 (2013).

43.   I. Y. Cha, S. H. Park, J. W. Lim, S. J. Yoo and Y.-E. Song, *Sol. Energy Mater. Sol. Cells* **108**, 22 (2013).

44.   H. J. Gläser, Large Area Glass Coating, von Ardenne Anlagentechnik GmbH, Dresden, Germany, 2000.

45.   R.-T. Wen, G. A. Niklasson and C. G. Granqvist, *ACS Appl. Mater. Interfaces* **7**, 9319 (2015).

46.   B. D. Cullity and S. R. Stock, Elements of X-Ray Diffraction, 3rd edition, Prentice-Hall, Upper Saddle River, NJ, USA, 2001.

47.   M. Mayer, *Am. Inst. Phys. Conf. Proc.* **475**, 541 (1999).

48.   E. Clementi and D. L. Raimondi, Atomic screening constants from SCF functions, *J. Chem. Phys.* **38**, 2686 (1963).

49.   Y. Liu, H. Masumoto and T. Goto, *Mater. Trans.* **45**, 3023 (2004).

50.   M. Peuckert, *Surf. Sci.* **144**, 451 (1984).

51.   M. Hara, K. Asami, K. Hashimoto, T. Masumoto, *Electrochim. Acta* **28**, 1073 (1983).

52.   G. Wei, b, Y. Wang, C. Huang, Q. Gao, Z. Wang, L. Xu, *Int. J. Hydrogen Energy* **35**, 3951 (2010).

53.   S. Kato, J. Jung, T. Suenobu, S. Fukuzumi, *Energy. Environ. Sci.* **6**, 3756 (2013).

54.   A. N. Mansour, *Surf. Sci. Spectra* **3**, 231 (1963).

55.   H.-L. Chen, Y.-M. Lu, J.-Y. Wu, W.-S. Hwang, *Mate. Trans.* **46**, 2530 (2005).

Table 1. Atomic composition γ of Ir–Ni oxide and Ni oxide thin films as determined by RBS.

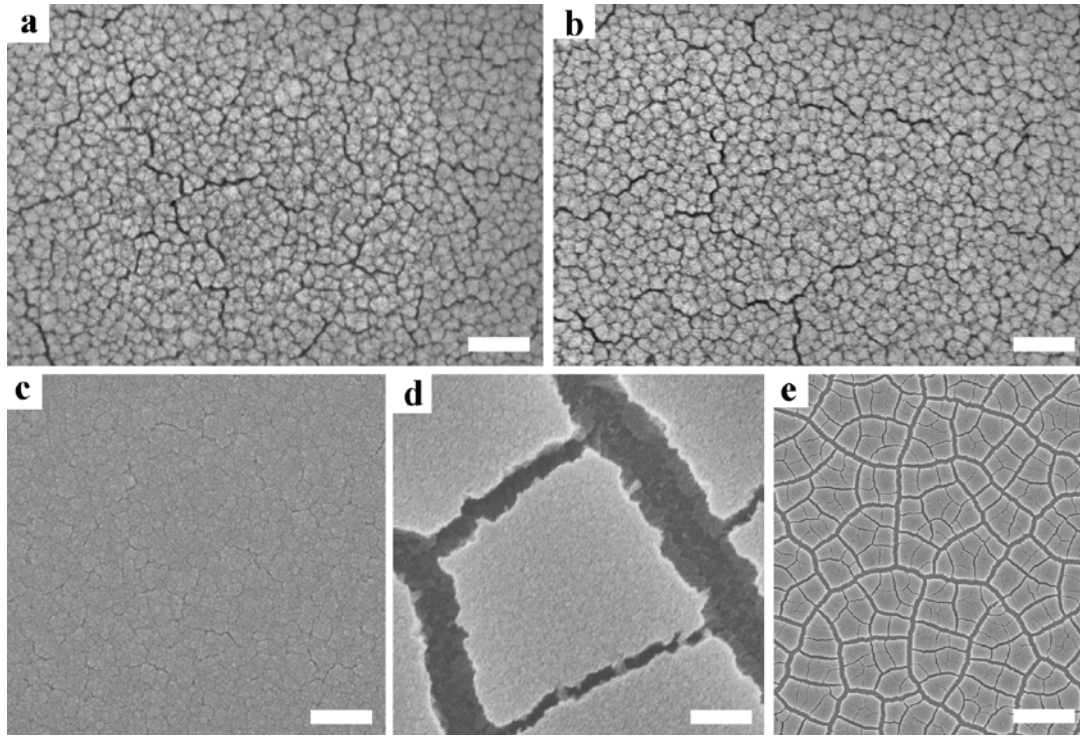| γ (%)	Composition
-	$NiO_{1.16}$
4.5	$Ir_{0.045}Ni_{0.955}O_{1.26}$
5.4	$Ir_{0.054}Ni_{0.946}O_{1.37}$
7.6	$Ir_{0.076}Ni_{0.924}O_{1.32}$
8.8	$Ir_{0.088}Ni_{0.912}O_{1.31}$
18.3	$Ir_{0.183}Ni_{0.817}O_{1.39}$

Figure 1. SEM images of ~300-nm-thick Ir–Ni oxide thin films before and after electrochemical cycling in the range 2.0–4.1 V *vs.* Li/Li$^+$ at 50 mV/s. (a) and (b) refer to a film with γ = 7.6% in initial stage and after 10,000 cycles, respectively. (c) and (d) refer to a film with γ = 18.3% in initial state and after 10,000 cycles, respectively. (e) is a de-magnified image of Fig. 1d. Scale bars are 200 nm for (a)–(d), and 1 μm for (e).
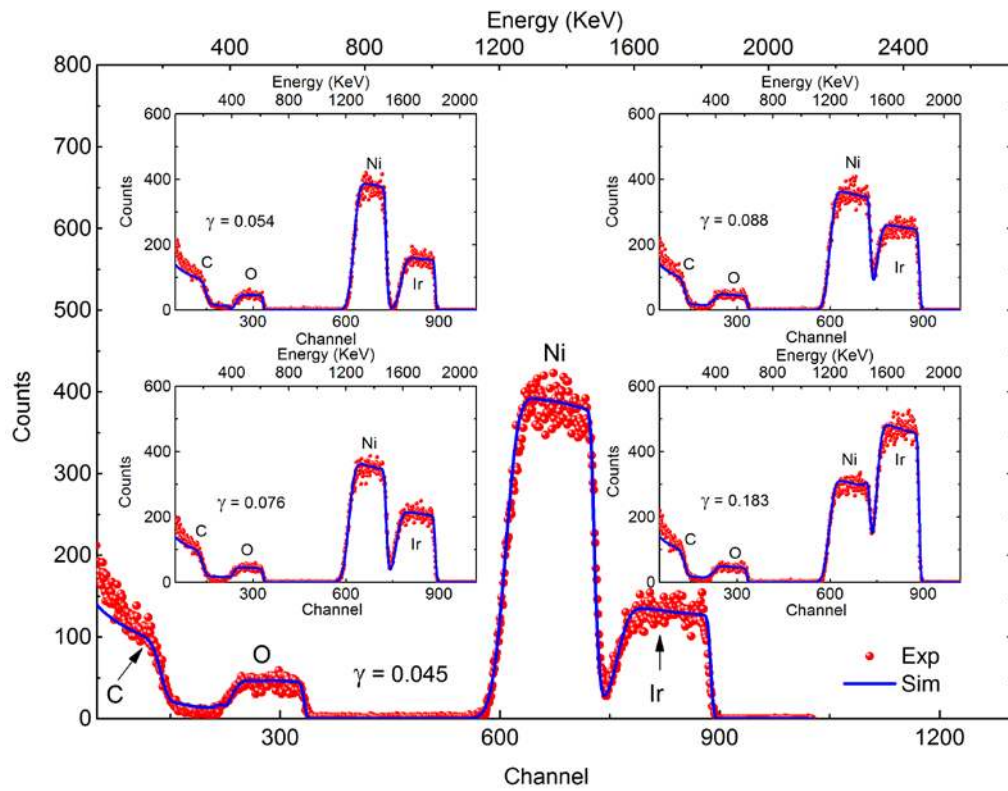
Figure 2. Experimental and simulated RBS spectra for ~300-nm-thick as-deposited Ir–Ni oxide thin films with various Ir concentrations γ. The substrates were carbon layers. Elemental compositions were determined by fitting experimental results (red dots) to simulated data (blue curves).
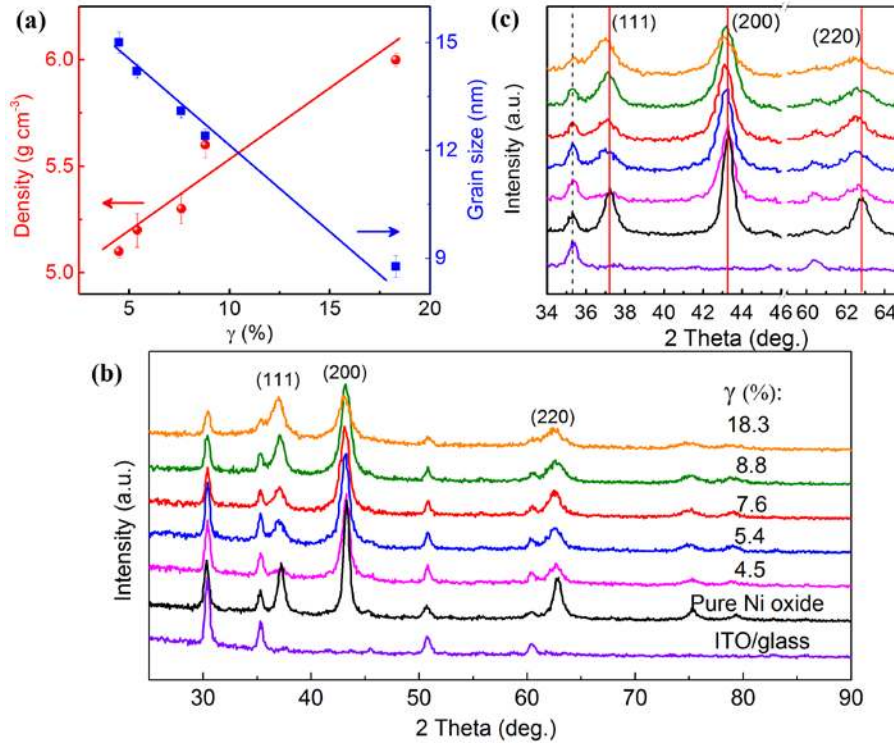
Figure 3. Structure analysis for as-deposited Ir–Ni oxide thin films with various Ir concentrations γ on ITO-coated glass. Film thicknesses were ~300 nm for Ir–Ni oxide films and ~250 nm for pure Ni oxide. (a) Film density and grain size D *vs*. Ir concentration. (b) X-ray diffractograms for Ir–Ni oxide thin films; data for ITO-coated glass and for pure Ni oxide are shown for comparison. (c) Enlarged diffraction features for the three main peaks. Vertical lines serve as guidance for the eye; red lines indicate shifts of the Ir–Ni oxide peaks, and black dashed line highlights that no similar effect takes place for ITO. Diffraction data are vertically displaced.
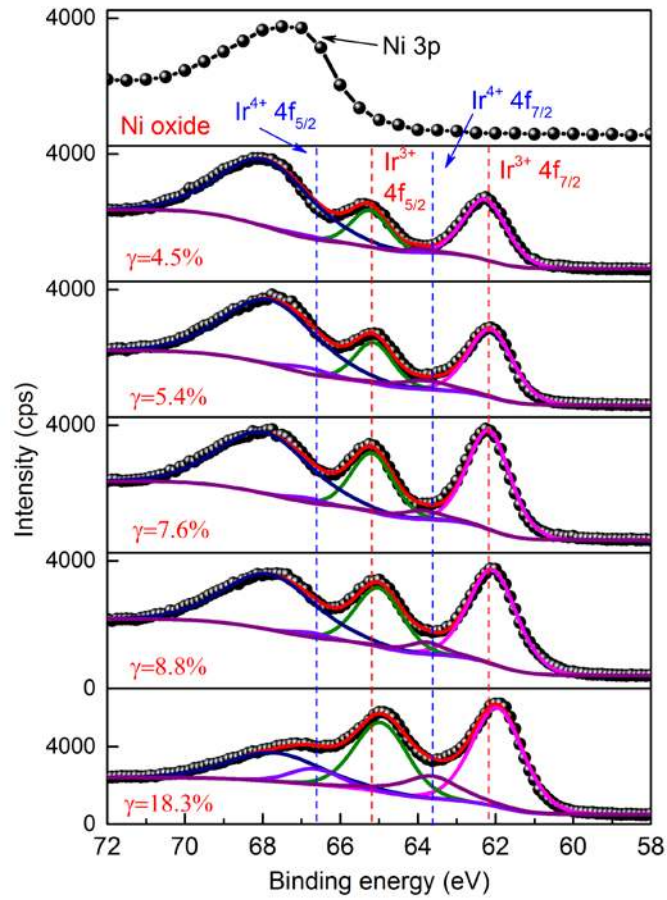
Figure 4. XPS spectra for a 250-nm-thick pure Ni oxide film and for ~300-nm-thick Ir–Ni oxide films with various Ir concentrations γ. After background subtraction, the features were fitted to Gaussian and Lorentzian curves and were assigned to the indicated states in Ir and Ni. Vertical lines indicate peak positions expected for Ir^{3+} and Ir^{4+}.
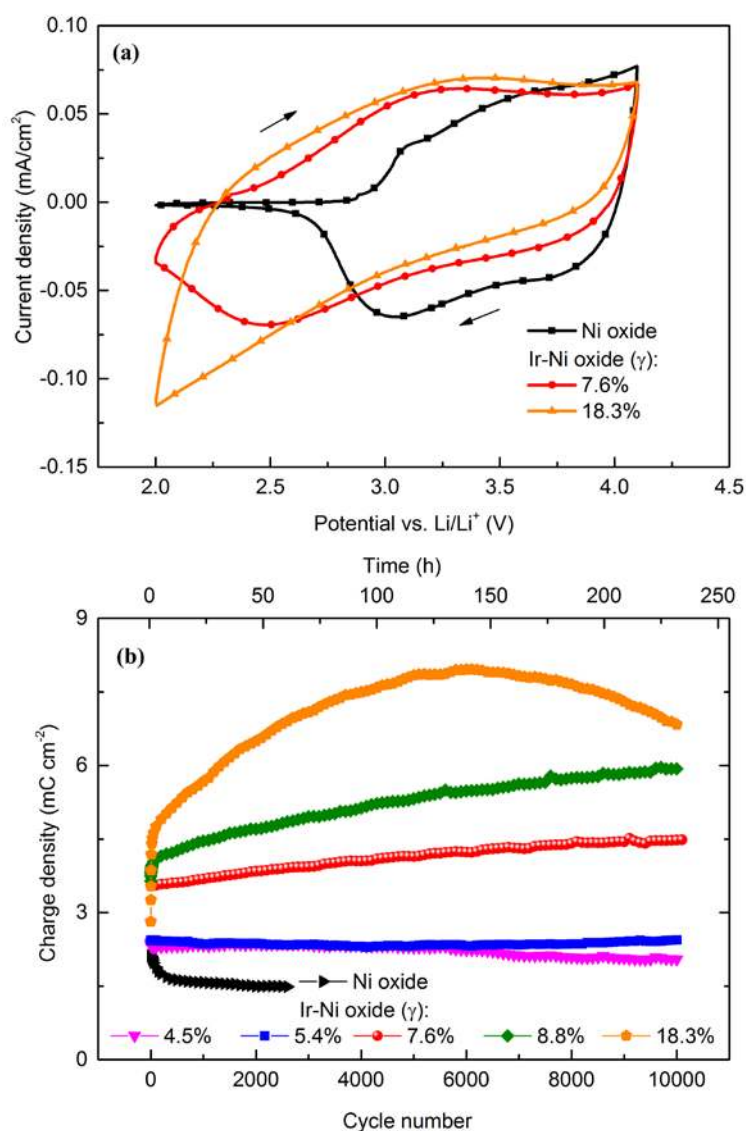
Figure 5. Electrochemical cycling durability for Ir–Ni oxide thin films with various Ir concentrations γ. (a) Cyclic voltammograms of Ni oxide and Ir–Ni oxide thin films after five CV cycles. (b) Charge density *vs*. cycle number. Cycling took place in the range 2.0–4.1 V *vs*. Li/Li$^+$ at 50 mV/s. Film thicknesses were ~300 nm for Ir–Ni oxide films and ~250 nm for pure Ni oxide.
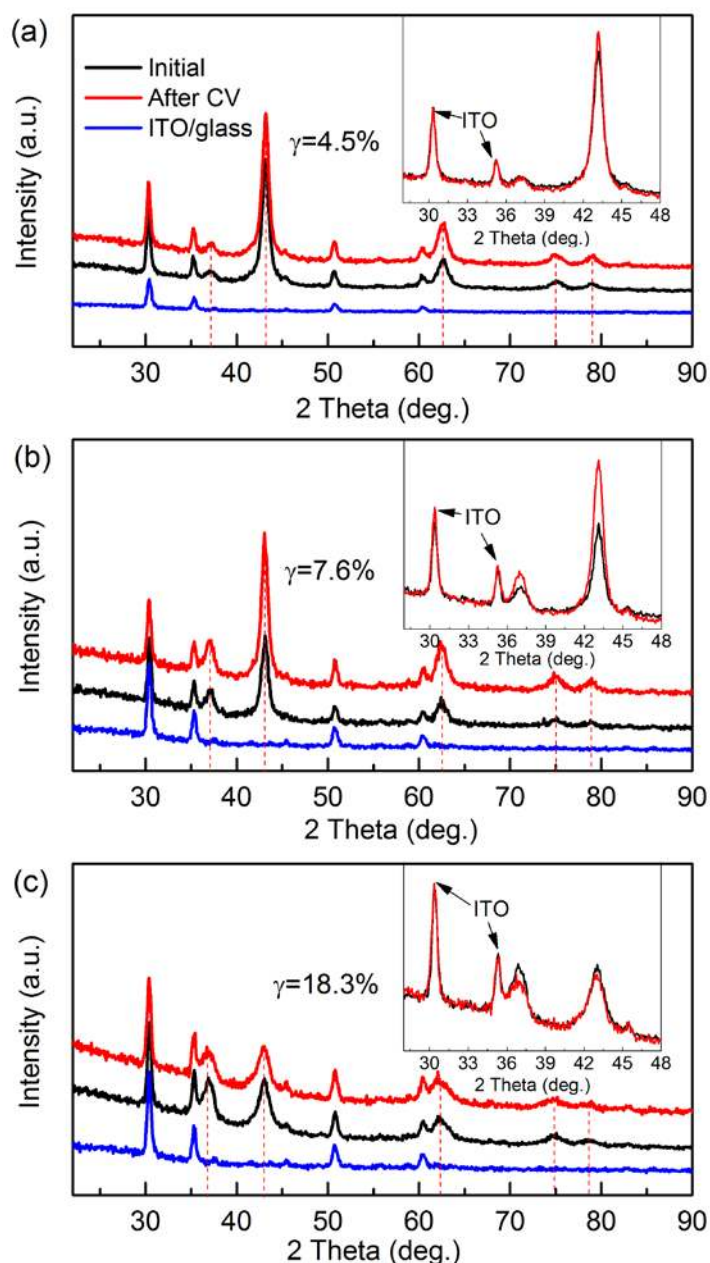
Figure 6. X-ray diffractograms for Ir–Ni oxide thin films with various Ir concentrations γ in as-deposited state and after 10,000 CV cycles. Data for an ITO-coated glass substrate are shown for comparison. Dashed vertical lines serve as guidance for the eye. The diffraction data are vertically displaced. The insets are close-ups between 28 and 48°. The diffraction intensities for ITO were barely altered after CV cycling, indicating that the different diffraction intensity from Ir–Ni oxide after CV cycling is due to changes of its crystallinity. Diffraction data are vertically displaced in the main panels.
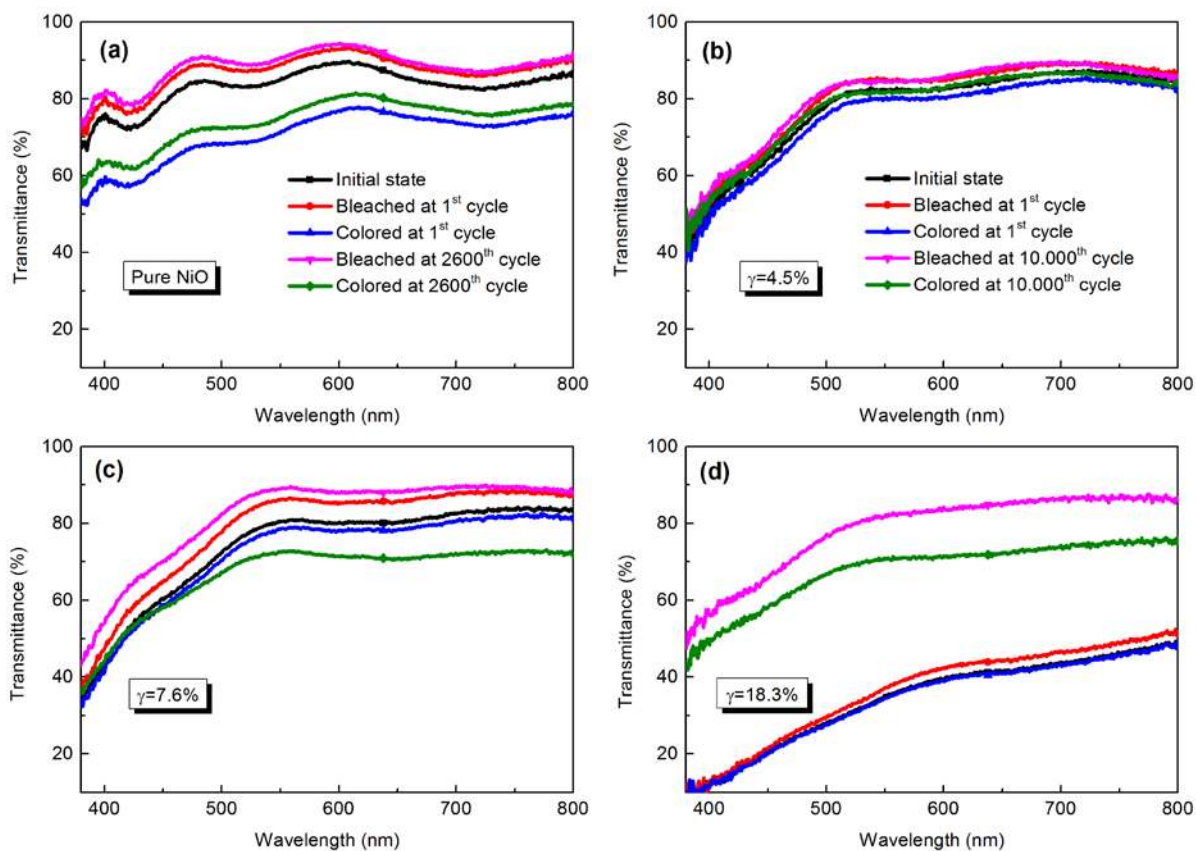
Figure 7. Spectral optical transmittance for a 250-nm-thick pure Ni oxide film and ~300-nm-thick Ir–Ni oxide films with various Ir concentrations γ. Data are shown for films in their as-deposited state and after bleaching and coloration upon CV cycling, for the shown number of cycles, in the range 2.0–4.1 V *vs*. Li/Li$^+$ at 50 mV/s. In (d), spectra for the as-deposited state and after the first coloration overlap.
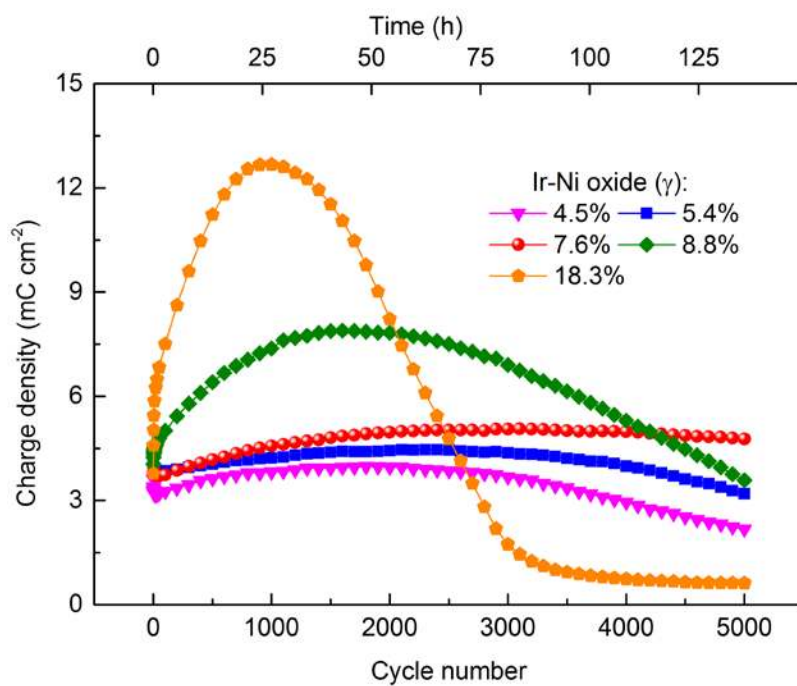
Figure 8. Charge density as a function of number of CV cycles between 2.0 and 4.4 V *vs.*

Li/Li$^+$ for ~300-nm-thick Ir–Ni oxide films with various Ir concentrations *γ*.